CHEMISTRY OF MATERIALS

Article

pubs.acs.org/cm

Photoluminescence Tuning via Cation Substitution in Oxonitridosilicate Phosphors: DFT Calculations, Different Site Occupations, and Luminescence Mechanisms

Guogang Li,[†,‡] Chun Che Lin,[†] Wei-Ting Chen,[†] Maxim S. Molokeev,[§] Victor V. Atuchin,[∥,▲,⬡] Chang-Yang Chiang,[⊥] Wuzong Zhou,[⊥] Chin-Wei Wang,[#] Wen-Hsien Li,[#] Hwo-Shuenn Sheu,[○] Ting-Shan Chan,[○] Chonggeng Ma,[△] and Ru-Shi Liu*[,†]

[†]Department of Chemistry, National Taiwan University, Taipei 106, Taiwan

[‡]Faculty of Materials Science and Chemistry, China University of Geosciences, Wuhan, 430074 Hubei, China

[§]Laboratory of Crystal Physics, Kirensky Institute of Physics, SB RAS, Krasnoyarsk 660036, Russia

[∥]Laboratory of Optical Materials and Structures, Institute of Semiconductor Physics, SB RAS, Novosibirsk 630090, Russia

[▲]Functional Electronics Laboratory, Tomsk State University, Tomsk 634050, Russia

[⊥]EaSTCHEM, School of Chemistry, St. Andrews University, St. Andrews, Fife KY16 9ST, United Kingdom

[#]Center for Neutron Beam Applications, National Central University, Zhongli 320, Taiwan

[○]National Synchrotron Radiation Research Center, Hsinchu 300, Taiwan

[△]College of Mathematics and Physics, Chongqing University of Posts and Telecommunications, Chongqing 400065, China

[⬡]Laboratory of Semiconductor and Dielectric Materials, Novosibirsk State University, Novosibirsk 630090, Russia

Supporting Information

ABSTRACT: Tuning and optimizing luminescent properties of oxonitridosilicates phosphors are important for white light-emitting diode (WLED) applications. To improve the color rendering index, correlated color temperature and thermal stability of layer-structured $MSi_2O_2N_2$:Eu (M = Sr, Ba) phosphors, cation substitutions have been used to adjust their luminescent properties. However, the underlying mechanisms are still unclear. In this research, a series of $(Sr_{1-x}Ba_x)Si_2O_2N_2$:Eu ($0 \le x \le 1$) compounds were prepared by solid-state reaction, after which systematic emission variations were investigated. The crystal structures of $(Sr_{1-x}Ba_x)Si_2O_2N_2$:Eu ($0 \le x \le 1$) are nominally divided into three sections, namely, Phase 1 ($0 \le x \le 0.65$), Phase 2 ($0.65 < x < 0.80$), and Phase 3 ($0.80 \le x \le 1$) based on the X-ray diffraction measurements. These experimental results are further confirmed by optimizing the crystal structure data with first-principle calculations. Continuous luminescence adjustments from green to yellow are observed in Phase 1 with gradual replacement of Sr^{2+} with Ba^{2+}, and the abnormal redshift is clarified through extended X-ray absorption fine structure analysis. Sr(Eu)−O/N bond length shrinkage in local structure causes the redshift emission, and the corresponding luminescence mechanism is proposed. Controllable luminescence in Phase 2 (from blue to white) and Phase 3 (from cyan to yellowish green) are observed. Based on the high-resolution transmission electron microscopy and selected area electron diffraction analysis, the two kinds of luminescence tuning are attributed to phase segregation. This study serves as a guide in developing oxonitride luminescent materials with controllable optical properties based on variations in local coordination environments through cation substitutions.

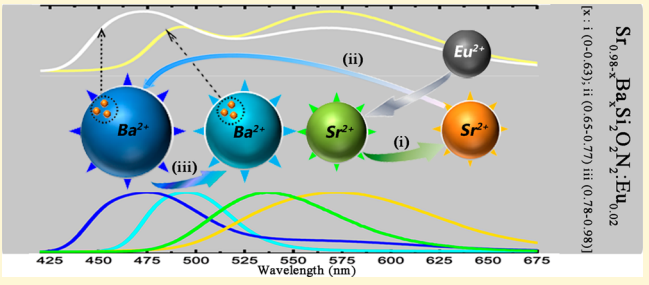

INTRODUCTION

White light-emitting diodes (WLEDs) are promising next-generation lighting alternatives to conventional incandescent and fluorescent lamps because of their energy efficiency, durability, reliability, and environmental friendliness.[1] Phosphors are efficient luminescent materials and indispensible components in generating white light in WLED devices; phosphors typically possess good thermal stability, high conversion efficiency, and strong absorption in the UV to blue region (380 to 460 nm).[2] The combination of a blue-emitting (460 nm) InGaN LED chip and yellow-emitting phosphor $Y_3Al_5O_{12}:Ce^{3+}$ is a widely utilized commercial WLED.[3] However, this type of white-light blending method has poor color rendering index (CRI; Ra = 70 to 80) and high

Received: March 10, 2014
Revised: April 2, 2014
Published: April 7, 2014

correlated color temperature (~7750 K), namely cool white light, because of the lack of red and green components in its spectrum.[3] To achieve "warmer" white light with high Ra, blue-LED and yellow-emitting phosphors with more spectra cover in red/green region or UV-LED (380 to 420 nm) and red, green, and blue (RGB) multicompositional phosphors are combined.[4] Developing highly efficient phosphors with tunable color points in the entire visible region under blue or UV light excitation and high thermal quenching temperatures is needed. The use of a single-compositional white phosphor instead of phosphor blends is another efficient way to improve WLEDs, which could reduce some variations in the phosphor blend.[5] This approach generally requires a controllable emission adjustment in complementary color regions and mixing to obtain white light.[5]

Activated rare-earth oxonitridosilicate compounds have been widely explored as advanced optical materials in WLED applications because they could produce a full spectrum of lighting under blue and/or UV light excitation.[2a,b,6] The presence of coordinated nitrogen not only increases the covalence of host lattices, thereby improving thermal stability, but also enhances crystal field splitting of Eu^{2+} or Ce^{3+} 5*d*, resulting in a shift of emission spectrum to long wavelength direction, thereby producing "warmer" white emission. Moreover, these phosphors can be synthesized under atmospheric conditions, resulting in a lower cost than nitridosilicate luminescent materials such as $M_2Si_5N_8$:Eu (M = Ca, Sr, Ba) and $MAlSiN_3$:Eu (M = Ca, Sr).[7] Among phosphor candidates, significant interest is being given to layered $MSi_2O_2N_2$:Eu (M = Ca, Sr, Ba).[8] In 2004, Schnick et al.[8] first reported about $MSi_2O_2N_2$ (M = Ca, Sr, Ba) compounds and then elucidated their real structure. In 2005, Li et al.[9] found that $MSi_2O_2N_2$ (M = Ca, Sr, Ba) have suitable host lattices for Eu^{2+}-doping, which show efficient yellow, green, and cyan emission, respectively, under blue and/or UV light excitation. Color point tuning is an efficient but difficult modus to improve CRI further and obtain excellent warm white light.[10] The present research in rare-earth ion-doped $MSi_2O_2N_2$ (M = Ca, Sr, Ba) phosphors mainly focuses on the development of an appropriate host composition and partial replacement of constituents to adjust their emission spectrum and optimize luminescent properties. Thus, far, cation substitutions have been considered as a promising approach. For example, Bachmann et al.[11] exhibited a tunable emission by changing Eu^{2+}-doping contents and replacing alkaline earth metal cations. Seibald et al.[12] observed highly efficient yellow and unexpected blue emissions in $(Sr_{0.5}Ba_{0.5})Si_2O_2N_2$:Eu and $(Sr_{0.25}Ba_{0.75})Si_2O_2N_2$:Eu, respectively. However, some underlying luminescence mechanisms are still unclear, and investigations are needed to clarify several issues. First, an abnormal redshift emission is found in $MSi_2O_2N_2$:Eu (M = Sr, Ba) with gradual substitution of Sr with Ba. The difference between the local coordination environments and the average structure of activator ions should be clarified.[11] Second, structure variation-induced continuous luminescent adjustments are present in $MSi_2O_2N_2$:Eu (M = Sr, Ba), so systematic observation and analysis are needed.[11,12] In addition, similar staggered arrangements of $(Si_2O_2N_2)^{2-}$ units and cations layers in the $(Sr_{1-x}Ba_x)Si_2O_2N_2$:Eu system underlie possible chemical tuning and phase segregation, providing a useful family of tunable luminescence based on different Eu^{2+} emission sites. To the best of our knowledge, no studies have been conducted about the design of white light emission in single Eu^{2+}-doped oxonitridosilicate hosts.

EXPERIMENTAL SECTION

Chemicals and Materials. $SrCO_3$ (≥99.9%), SiO_2 (≥99.995%), Si_3N_4 (≥99.9%), and Eu_2O_3 (≥99.99%) were purchased from Aldrich Corporation. $BaCO_3$ (≥99.9%) was purchased from J.T. Baker Corporation. All of the initial chemicals were used without further purification. Aluminum oxide crucibles and cylindrical molybdenum crucibles (Φ20 mm × 50 mm) were used in the sintering process of the samples.

Synthesis. A series of oxonitridosilicate compounds, $(Sr_{1-x}Ba_x)Si_2O_2N_2$:Eu ($0 \le x \le 1$), was prepared using two-step solid-state reaction processes. Nonstoichiometric amounts of $SrCO_3$, $BaCO_3$, SiO_2, and Eu_2O_3 powders, in which the molar ratio of (Sr, Ba)/Si = 0.8,[6g] were ground in an agate mortar for 30 min to form a homogeneous mixture. The mixture was then placed in aluminum oxide crucible and fired at 1250 to 1350 °C for 6 h under flowing 95% N_2−5% H_2 atmosphere in a horizontal tube furnace. The sintered products were ground, yielding crystalline powder $(Sr_{1-x}Ba_x)_2Si_{0.8}O_4$:Eu ($0 \le x \le 1$). The crystalline powder was mixed with stoichiometric amounts of Si_3N_4 and reground for 30 min in an agate mortar. After forming a homogeneous mixture, the mixture was loaded into a cylindrical molybdenum crucible with a screw-cap and fired again at 1500 to 1550 °C for 6 h under flowing 95% N_2−5% H_2 atmosphere in the horizontal tube furnace. The second sintered products were ground again, yielding the resulting phosphor powder.

Characterization. Finely ground powders were used in all of the measurements. The phase purity of all samples were analyzed using synchrotron X-ray diffraction (XRD) with wavelength λ = 0.774907 Å and a Debye−Scherrer camera installed at the BL01C2 beamline of the National Synchrotron Radiation Research Center (NSRRC), Taiwan. Neutron powder diffraction (NPD) data from the $(Sr_{0.25}Ba_{0.73}Eu_{0.02})Si_2O_2N_2$ sample was obtained with the use of a high-resolution diffractometer HRPD at ANSTO, Australia. NPD and XRD Rietveld profile refinements of the structural models and texture analysis were performed with the use of General Structure Analysis System (GSAS) and TOPAS 4.2[13] software. Solid-state nuclear magnetic resonance (NMR) spectra were obtained with the use of a Bruker DSX 300 MHz NMR spectrometer, equipped with 4 mm double-resonance magic-angle-spinning (MAS) probe. High-resolution transmission electron microscopy (HRTEM) and selected area electron diffraction (SAED) images were obtained with the use of JEOL JEM-2011 microscope operated at 200 kV. Photoluminescence (PL) spectra were obtained using a FluoroMax-3 spectrophotometer equipped with a 150 W Xe lamp and a Hamamatsu R928 photomultiplier tube. A THMS-600 heating device was added to study thermal quenching. The Sr K-edge extended X-ray absorption fine structure (EXAFS) spectrum was obtained under transmission mode for a sample mounted on Scotch tape at BL01C1 beamline of the NSRRC. The incident (I_0) and transmitted (I) beam intensities were measured by gas ionization chambers filled with 55%N_2 and 20%Ar gas mixture and 50%Ar and 30%Kr gas mixture, respectively. The analytical program "Artemis" for curve fitting was utilized to perform the EXAFS analyses.

Computational Method. DFT calculations were performed to study the structural and electronic properties of three phases, namely, $SrSi_2O_2N_2$, $(Sr_{0.25}Ba_{0.75})Si_2O_2N_2$, and $BaSi_2O_2N_2$ using the periodic first-principle CRYSTAL09 code[14] based on the linear combination of atomic orbitals (LCAO) method. The hybrid exchange-correlation functional WC1PBE consisting of a PBE correlation part and a Wu−Cohen exchange part with a fractional mixing (16%) of the nonlocal Hartree−Fock (HF) exchange[15] was employed to yield better agreement between the calculated and experimental electronic properties of solids. The local Gaussian-type basis sets (BSs) for the three phases were chosen as follows: the all-electron BSs in the form of 86-311G*, 8-411G*, and 6-31G* were used for Si, O, and N atoms,[16] respectively; for Sr and Ba atoms, the Hay−Wadt small-core pseudopotentials and their related valence BSs from ref 17 were adopted. The Monkhorst−Pack scheme for 8 × 8 × 8 *k*-point mesh in the Brillouin zone was applied. The truncation criteria for bielectronic integrals (Coulomb and HF exchange series) were correspondingly set to 8, 8, 8, 8, and 16.[14] A predefined "extra large" pruned DFT

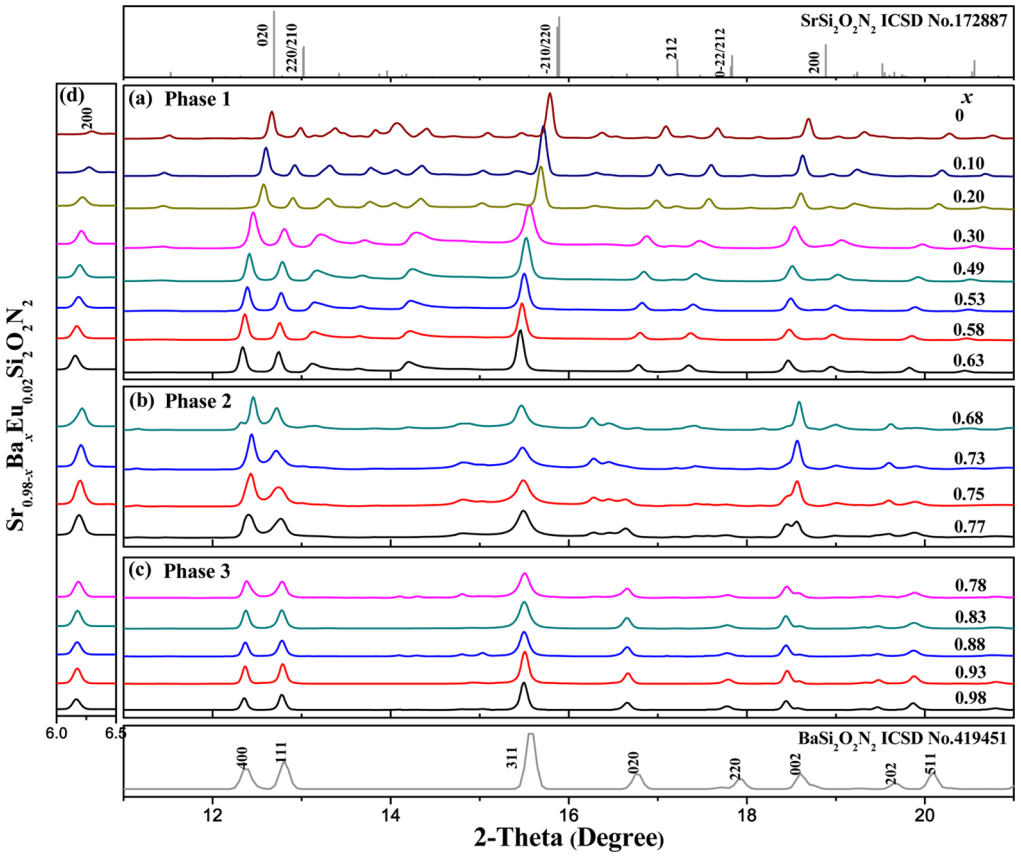

Figure 1. XRD patterns of the as-prepared $(Sr_{0.98-x}Ba_xEu_{0.02})Si_2O_2N_2$ samples. (a) x = 0 to 0.63 [Phase 1: Triclinic ($P1$)]. (b) x = 0.68 to 0.77 [Phase 2: Triclinic ($P1$)]. (c) x = 0.78 to 0.98 [Phase 3: Orthorhombic ($Pbcn$)]. The standard data of $SrSi_2O_2N_2$ (ICSD No. 172877) and $BaSi_2O_2N_2$ (ICSD No. 419450) are used as references.

Table 1. Crystallographic Parameters Obtained from XRD Rietveld Refinements for $(Sr_{0.98-x}Ba_xEu_{0.02})Si_2O_2N_2$[a]

	crystallographic parameter							reliability factors	
$(Sr_{0.98-x}Ba_xEu_{0.02})Si_2O_2N_2$	a (Å)	b (Å)	c (Å)	α (deg)	β (deg)	γ (deg)	V (Å^3)	R_{wp} (%)	R_p (%)
Phase 1: Triclinic ($P1$), Impurity in All of the Samples <5%, Isostructural to $SrSi_2N_2O_2$									
x = 0	7.101(4)	7.252(4)	7.278(5)	88.77(1)	84.75(4)	75.91(9)	362.02(8)	9.76	7.55
x = 0.10	7.127(7)	7.279 (7)	7.297(7)	88.71(7)	84.69(3)	75.87(7)	365.55(6)	11.89	8.92
x = 0.20	7.139(8)	7.292(9)	7.302(8)	88.71(7)	84.66(3)	75.8(9)	367.07(7)	11.01	8.26
x = 0.30	7.161(6)	7.314(5)	7.323(7)	88.66(4)	84.55(6)	75.89(6)	370.37(2)	10.68	7.94
x = 0.40	7.200(2)	7.361(2)	7.318(2)	88.62(2)	84.46(7)	75.88(1)	374.32(2)	10.21	7.78
x = 0.49	7.208(2)	7.390(2)	7.336(2)	88.64(1)	84.47(7)	75.88(8)	377.11(1)	12.62	9.46
x = 0.53	7.214(2)	7.402(2)	7.341(2)	88.64(1)	84.46(7)	75.89(8)	378.46(2)	13.96	10.38
x = 0.58	7.223(2)	7.417(2)	7.347(2)	88.65(1)	84.45(8)	75.90(8)	379.90(2)	14.49	11.12
x = 0.63	7.228(2)	7.429(2)	7.352(2)	88.65(1)	84.42(7)	75.92(8)	381.08(2)	15.10	11.19
Phase 2: Triclinic ($P1$), Impurity in 0.68 and 0.73 Samples <5%; in 0.75 and 0.77 Samples >10%, Isostructural to $(Sr_{0.25}Ba_{0.75})Si_2N_2O_2$									
x = 0.68	4.780(1)	5.477(2)	14.275(5)	89.55(5)	90.02(2)	89.71(3)	375.02(2)	8.48	5.48
x = 0.75	4.804(5)	5.462(5)	14.302(1)	89.70(9)	90.04(5)	89.59(5)	375.16(6)	7.76	5.11
x = 0.77	4.809(7)	5.449(6)	14.272(2)	89.61(7)	90.1(1)	89.32(9)	373.81(8)	7.13	4.55
Phase 3: Orthorhombic ($Pbcn$), Impurity in All Samples <5%, Isostructural to $BaSi_2N_2O_2$									
x = 0.83	14.385(1)	5.353(5)	4.838(3)	90	90	90	372.53(5)	11.12	7.69
x = 0.88	14.387(2)	5.350(7)	4.836(6)	90	90	90	372.25(8)	18.36	11.45
x = 0.93	14.391(1)	5.347(4)	4.833(4)	90	90	90	371.83(5)	14.28	9.60
x = 0.98	14.392(1)	5.349(4)	4.835(3)	90	90	90	372.37(4)	16.07	9.96

[a]**Additional information**: Strong anisotropic broadening of diffraction peaks in $(Sr_{1-x}Ba_xEu_{0.02})Si_2N_2O_2$ (x = 0.30 to 0.63) is detected, which may be induced by lattice strain, anisotropic particle shape, or staking faults.

integration grid (i.e., XLGRID) was adopted together with much higher DFT density and grid weight tolerances (values 8 and 16).[14] The tolerance of the energy convergence on the self-consistent field iterations (TOLDEE) was set to 10^{-8} hartree, and the convergence speed was facilitated by mixing 40% of the Hamiltonian matrix in the last cycle into the current cycle. In the geometry optimization

dx.doi.org/10.1021/cm500844v | Chem. Mater. 2014, 26, 2991−3001

calculation, the convergence criteria on the root-mean-square of the gradient and the nuclear displacement (TOLDEG and TOLDEX) were set to 0.00006 hartree/bohr and 0.00012 bohr, respectively. The maximum allowed gradient and displacement were 1.5× as large, i.e., 0.00009 hartree/bohr and 0.00018 bohr. The optimized structural data with higher accuracy were used to confirm the validity of the Rietveld refinement from the XRD patterns of the three phases. The electronic band structures and density of state (DOS) diagrams for the three phases were calculated based on the fully optimized geometry structures.

RESULTS AND DISCUSSION

Crystal Phase, XRD Refinement, and Lattice Parameters. Previous studies[6c,8a] have reported the typical layer structure of $MSi_2O_2N_2$ (M = Sr, Ba), in which $(Si_2O_2N_2)^{2-}$ anions and cations are alternately arranged. $(Si_2O_2N_2)^{2-}$ anions consist of highly dense and vertex-sharing $SiON_3$ tetrahedra. Each N atom is linked with three Si atoms, and each O atom is terminally connected with two Si atoms. The $(Si_2O_2N_2)^{2-}$ anions in $SrSi_2O_2N_2$ have orthorhombic symmetry, whereas Sr cations exhibit a pseudohexagonal structure, resulting in a low symmetry (*P1*). There are four different Sr^{2+} crystallographic sites in the triclinic $SrSi_2O_2N_2$ unit cell, and each Sr^{2+} ion is coordinated with six O and two N atoms to form a trigonal prism.[8b] $EuSi_2O_2N_2$ is isotypic to $SrSi_2O_2N_2$, and thus, a completely solid solution $(Sr/Eu)Si_2O_2N_2$ is formed.[11,18a] $BaSi_2O_2N_2$ shows an orthorhombic unit cell with space group *Pbcn*. Moreover, only one crystallographic site is found for Ba^{2+} in the unit cell, which can be depicted as a cuboid coordinated with eight O plus two long-ranged N atoms.[8c]

The phase purity and structural type of the as-prepared $(Sr_{0.98-x}Ba_xEu_{0.02})Si_2O_2N_2$ samples were investigated using XRD. The synchrotron XRD data (Figure 1) show that the studied samples should be divided into three sections [phase 1 (x = 0 to 0.63), phase 2 (x = 0.68 to 0.77, and phase 3 (x = 0.78 to 0.98)] on the basis of the difference in position and relative intensity of the diffraction peaks. Moreover, the representative high-resolution XRD patterns recorded over the local angle range (11°−18°) for $(Sr_{0.98-x}Ba_xEu_{0.02})Si_2O_2N_2$ clearly illustrate that there are three different phases because of obviously different diffraction peaks in the three phases, as shown in Figure S1 (Supporting Information). Rietveld refinements from XRD patterns of phase 1 and 3 series confirm that these compounds are single phase and isostructural to known crystal structures of $SrSi_2O_2N_2$ and $BaSi_2N_2O_2$, respectively.[8b,c] The Eu as isotropic displacement factors for Sr/Ba atoms in $(Sr_{0.98-x}Ba_xEu_{0.02})Si_2O_2N_2$ were constrained to be equal. Detailed refinement parameters are listed in Table 1. The diffraction peaks of $(Sr_{0.98-x}Ba_xEu_{0.02})Si_2O_2N_2$ (x = 0 to 0.63) samples that are consistent with the literature values (ICSD No.172877) can be easily assigned to the triclinic phase of $SrSi_2O_2N_2$ (space group *P1*, Figure 1a). Given that the ion radius of Sr^{2+} (1.21 Å, CN = 7)[19] is smaller than Ba^{2+} (1.38 Å, CN = 7)[19] in isostructural $SrSi_2O_2N_2$, an obvious shifting to lower 2θ direction of all of the diffraction peaks in phase 1 series (Figure 1a) can be observed with increasing x from 0 to 0.63. This phenomenon verifies the incorporation of Ba into the lattice. Smooth increases in lattice parameters (a, b, c, and V) with increasing x [Figures 2(a−c, e)] demonstrate that $(Sr_{0.98-x}Ba_xEu_{0.02})Si_2O_2N_2$ (x = 0 to 0.63) solid solutions are formed according to the Vegard rule.[18b] At x > 0.20, the anisotropic peak broadening is detected, which may be induced by lattice strain, anisotropic particle shape, or staking faults. The XRD patterns of phase 3 series (Figure 1c) are consistent

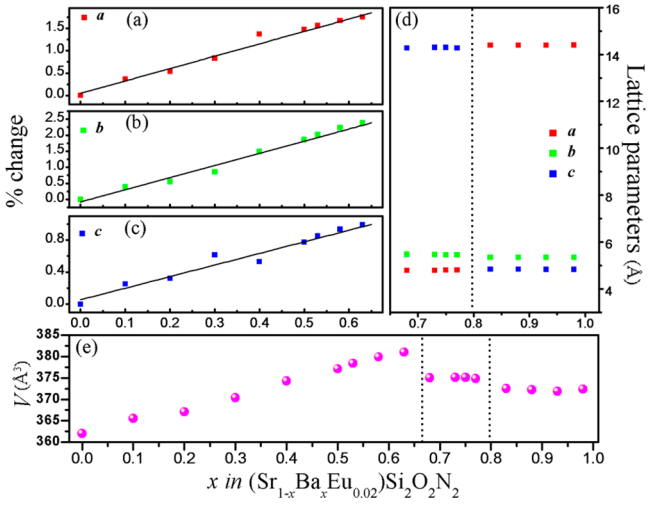

Figure 2. Structural results for $(Sr_{0.98-x}Ba_xEu_{0.02})Si_2O_2N_2$ samples. (a)−(c) Relative shifts in the lattice parameters with x = 0−0.63. (d) Lattice parameters of x = 0.68−0.77 samples. The series of samples with x = 0.68−0.77 have pseudo-orthorhombic parameters $a_t = c_o$, $b_t = b_o$, $c_t = a_o$ for the triclinic series cells (t, o subscripts) for direct comparison with the orthorhombic Ba series. (e) Cell volumes of x = 0−0.98 samples.

with standard $BaSi_2O_2N_2$ (ICSD No. 419450). The refinement results show that they are all pure orthorhombic phase (*Pbcn*) at x = 0.78 to 0.98 in $(Sr_{0.98-x}Ba_xEu_{0.02})Si_2O_2N_2$. Although it is difficult to see Vegard type dependence of the unit cell volume on nominal Ba content (because the slope of this dependence is small and the spreading of points are within only 8σ), phase 3 may be a solid solution with small structural parameters variation. Structural schematic diagrams perpendicular to the

Scheme 1. Structural Schematic Diagrams Perpendicular to the Stacking Direction of $(Sr_{0.98-x}Ba_xEu_{0.02})Si_2O_2N_2$ Structures[a]

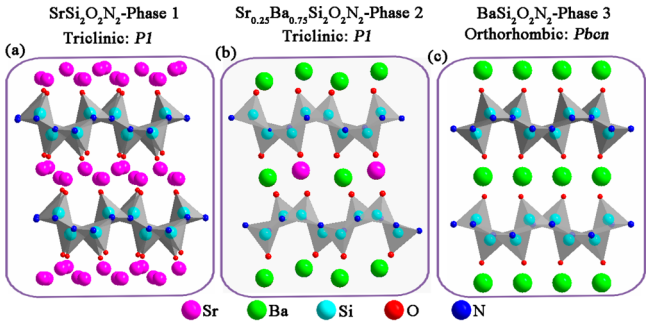

[a](a) Phase 1 (x = 0 to 0.63). (b) Phase 2 (x = 0.68 to 0.77). (c) Phase 3 (x = 0.78 to 0.98). Silicate layers of condensed $SiON_3^-$ tetrahedra (gray), Sr atoms (magenta), Ba atoms (green), Si atoms (cyan), O atoms (red), and N atoms (blue).

stacking direction of phase 1 and phase 3 are shown in Scheme 1a and 1c, respectively.

For phase 2 series (x = 0.68 to 0.77), more significant changes in position and relative intensity of diffraction peaks are found compared with those of phase 1 and phase 3 series (Figure 1b), which are probably caused by some differences in crystal structure. Seibald et al.[12b] reported that the crystal structure of $(Sr_{0.25}Ba_{0.75})Si_2O_2N_2$:Eu is attributed to the *P1*

dx.doi.org/10.1021/cm500844v | Chem. Mater. 2014, 26, 2991−3001

space group based on single crystal data analysis, as well as HRTEM and SAED results. However, detailed values of the crystallographic parameters were not given, particularly the coordination environment around the cations (Ba^{2+}, Sr^{2+}, Eu^{2+}), which is closely related to luminescent properties of Eu^{2+}. The cation distribution and coordination environment in

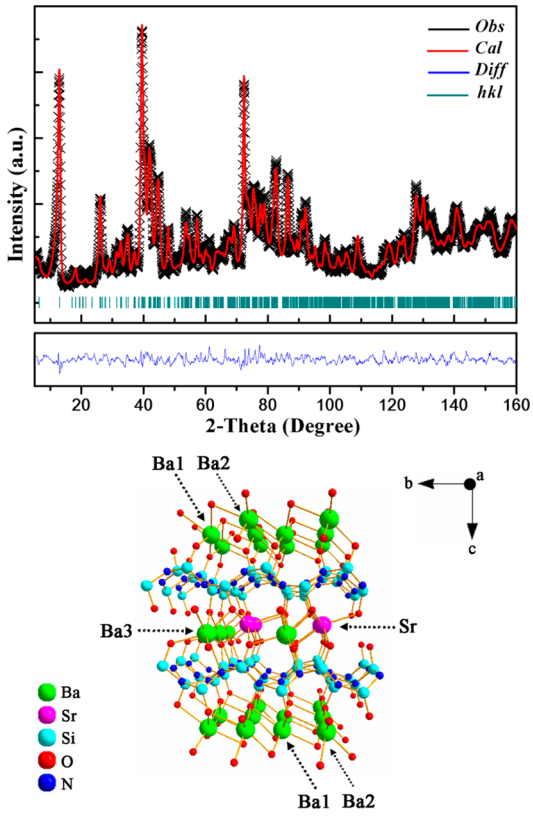

Figure 3. Fit to time-of-flight NPD data for $(Sr_{0.25}Ba_{0.73}Eu_{0.02})Si_2O_2N_2$. Structure refinement shows that three Ba sites and one Sr site exist in the lattice.

phase 2 series are determined by NPD analysis for representative $(Sr_{0.25}Ba_{0.73}Eu_{0.02})Si_2O_2N_2$. Figure 3 shows that the experimental data are consistent with the calculated data from the NPD refinement based on *P1* symmetry, indicating that $(Sr_{0.25}Ba_{0.73}Eu_{0.02})Si_2O_2N_2$ is a triclinic crystal phase with the following lattice parameters: a = 4.7967(5) Å, b = 5.4700(5) Å, c = 14.296(2) Å, α = 89.87(1)°, β = 89.88(1)°, γ = 90.00(1)°, and V = 375.11(8) Å^3. The crystallographic parameters are shown in Table 2, and other parameters such as coordinates of atoms and geometric parameters are shown in Tables S1 and S2 (Supporting Information), respectively. Phase 2 series shows crystal structures similar to those of $(Sr_{0.25}Ba_{0.73}Eu_{0.02})Si_2O_2N_2$ (Table 1). Although phase 2 series are triclinic crystal phase (*P1*), they have pseudo-orthorhombic parameters $a_t = c_o$, $b_t = b_o$, $c_t = a_o$ (t, o subscripts) for the direct comparison with the orthorhombic Ba series (Phase 3), as shown in Figure 2d. Furthermore, Figure 2(d, inset) and Table S2 show four cation sites (three Ba sites, one Sr site) in phase 2. The schematic structure of phase 2 is shown in Scheme 1b and Figure S2 (Supporting Information, *a* and *c* axes are exchanged in Figure S2 compared with Scheme 1b). Ba1 site is coordinated with six O and one N with long-range distance d(Ba−N) = 3.22(1) Å, which is a type of contact, not a bond. The Ba3 atom is coordinated with six O atoms and one N

Table 2. Crystallographic Parameters Obtained from NPD Refinement for $(Sr_{0.25}Ba_{0.73}Eu_{0.02})Si_2O_2N_2$

space group	*P1*
a, Å	4.7967(5)
b, Å	5.4700(5)
c, Å	14.296(2)
α, °	89.87(1)
β, °	89.88(1)
γ, °	90.00(1)
V, Å^3	375.11(8)
Z	1
2θ-interval, °	5 to 163
number of reflections	1432
number of parameters of refinement	166
number of constrains	51
R_{wp}, %	4.768
R_p, %	3.695
χ^2	1.304
R_B, %	1.369

atom, which are similar to those of the Sr site in $SrSi_2O_2N_2$ (Phase 1). The Ba2 atom is coordinated with six O atoms, five of the d(Ba−O) distances locate the range of 2.5−3.06(3) Å, which satisfies the definition of bond length within 3σ interval. The Ba2 also has contact with N at a distance of d(Ba−N) = 3.27(3) Å. The Sr atom is coordinated with six O atoms and one N with d(Sr−N) = 3.39(3) Å. Therefore, all of the cations in phase 2 (Ba1, Ba2, Ba3, and Sr) have six O and one N coordinations, which are similar to phase 1. However, some

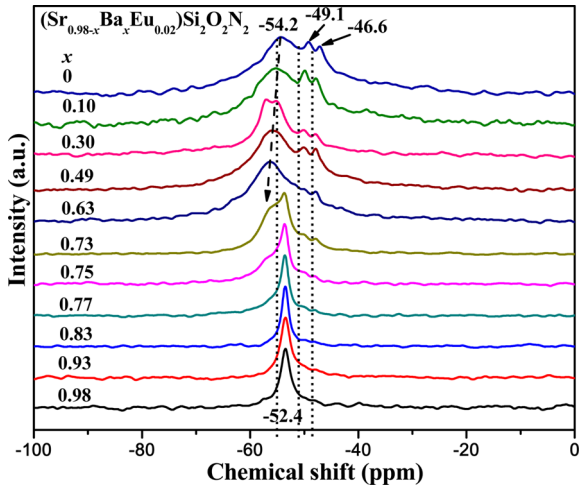

Figure 4. ^{29}Si solid-state NMR spectra of $(Sr_{0.98-x}Ba_xEu_{0.02})Si_2O_2N_2$ (x = 0 to 0.98) samples.

distortions are observed because of the relatively large ionic radius of the Ba cation. Figure 4 shows the ^{29}Si solid-state NMR spectra of $(Sr_{0.98-x}Ba_xEu_{0.02})Si_2O_2N_2$ (x = 0 to 0.98) samples. A group of closely adjoined signals from δ = −45 ppm to −54 ppm in all samples are attributed to the typical chemical shifts of Q^3-type $SiON_3$ tetrahedrons.[8a,20] A sharp, single peak at −52.4 ppm in $(Sr_{0.98-x}Ba_xEu_{0.02})Si_2O_2N_2$ (x = 0.83 to 0.98) samples show the presence of only one Si position in the phase 3 structure, which demonstrates that the low Sr substitution content does not change the crystal structure of phase 3 series. So it should be a solid solution phase except for small structural parameters variation. This is consistent with the previous XRD

dx.doi.org/10.1021/cm500844v | *Chem. Mater.* 2014, 26, 2991−3001

result (Figure 1c). A series of peaks, such as those at ∼−54, −49.1, and −46.6 ppm, indicate existence of different Si positions in $(Sr_{0.98-x}Ba_xEu_{0.02})Si_2O_2N_2$ (x = 0 to 0.63) samples (Phase 1) because of the low-symmetry triclinic structure. Moreover, the chemical shift of Si has slight shifts with the increase of Ba content, indicating different distortions of crystal structure. This phenomenon mainly results from the difference in ion radius of Sr^{2+} and Ba^{2+} ions. Interestingly, the $(Sr_{0.98-x}Ba_xEu_{0.02})Si_2O_2N_2$ (x = 0.63, 0.75, 0.77) samples simultaneously contain Si positions of phases 1 and 3 (Figure 4). Therefore, the Sr/Ba cations in phase 2 may possess the distortions that are different from those in phases 1 and 3 at the current doping level. This confirms that phase 2 is a new crystal structure that is different from phases 1 and 3, which is consistent with the previous report.[12b] Therefore, the ^{29}Si solid-state NMR results confirm the existence of three crystal structures with the increase of x, which are consistent with the XRD results.

Based on the Rietveld refinement results (Table 1) and ^{29}Si solid-state NMR spectra, $(Sr_{0.98-x}Ba_xEu_{0.02})Si_2O_2N_2$ generally show one of the three different crystal structures according to varying x value (phases 1, 2, and 3). The corresponding structural schematic diagrams perpendicular to the stacking direction are shown in Scheme 1. Phase 1 series (x = 0 to 0.63) are isostructural to triclinic $SrSi_2O_2N_2$, and a solid solution is formed. Phase 3 series (x = 0.78 to 0.98) have an identical orthorhombic phase with $BaSi_2O_2N_2$. It also presents a solid solution but with some local distortions. Phase 2 series represents a "new" crystal structure, which have three Ba sites and one Sr site in the lattice.[12b] This change of the coordination environment around cations may have a significant effect on Eu^{2+} luminescence, which is discussed in the PL section. In addition, the crystal structural data for the three phases were further optimized by the first-principle calculations (Tables S3 to S5, Supporting Information). Those data show consistency between the calculated and experimental crystal structures, confirming the rationality of our experimental analyses.

Electronic Structures of the Three Phases. Figure S3 (Supporting Information) shows the calculated band structures for the three phases. The calculated band gaps are equal (in eV) to 6.6(4), 6.6(8), and 6.6(3), which are direct characteristics of $SrSi_2O_2N_2$, $Ba_{0.75}Sr_{0.25}Si_2O_2N_2$, and $BaSi_2O_2N_2$, respectively. We believe that the calculated band gap values should be significantly close to the experimental values because of the use of the hybrid exchange-correlation functionals. Figure S3 also shows that the upper valence band (VB) states for all the three phases are relatively flat, whereas the strong dispersion of the highest conduction band (CB) states in the three phases results in a variable range of the band-to-band transition energies (∼6.6 to 7.5 eV). Assignment of the electronic bands can be performed on the basis of the calculated partial and total DOS (PDOS/TDOS) diagrams (Figure S4, Supporting Information). The VBs start around the Fermi level at 0 eV and decay near −8.5 eV for the three phases, and they are predominately derived from the O-p and N-p states. Moreover, the outermost core band can be observed at approximately −10 eV for the last two phases because of the relatively shallow Ba-p states compared with the Sr-p states. The CBs for all of the phases stretch from ∼8 to 15 eV, which are basically composed of the mixture of the metal cation d states and the Si-p states.

Photoluminescence (PL) Properties. Figure 5 shows the excitation and emission spectra of the $(Sr_{0.98-x}Ba_xEu_{0.02})Si_2O_2N_2$ samples. The excitation spectra in Figure 5a show that

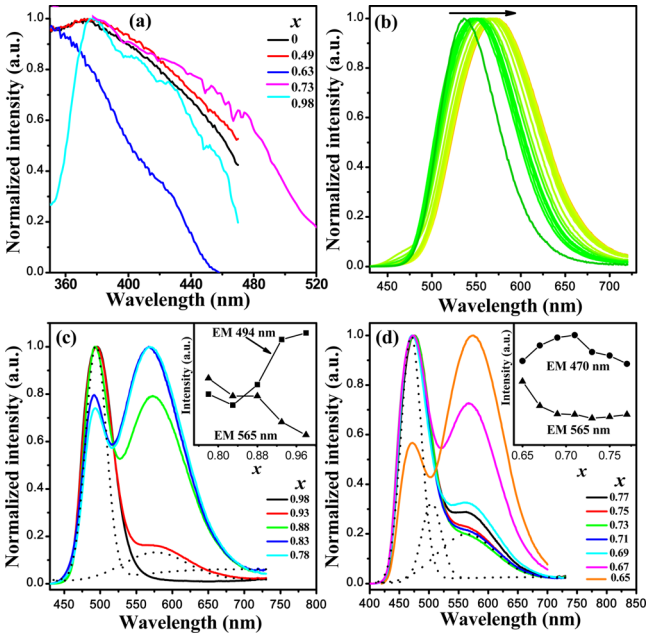

Figure 5. Typical PL excitation spectra of $(Sr_{0.98-x}Ba_xEu_{0.02})Si_2O_2N_2$ samples: (a) x = 0, 0.49, 0.63, 0.75, 0.98. PL emission spectra (λ_{ex} = 405 nm): (b) x = 0 to 0.63; (c) x = 0.65 to 0.77; (d) x = 0.78 to 0.98. The relative emission intensities at 470, 494, and 565 nm of the as-prepared samples as functions of x are shown as insets in (c) and (d). Black dotted lines in parts (c) and (d) show Gaussian fitting curves of x = 0.73 and x = 0.93 samples, respectively.

$(Sr_{0.98-x}Ba_xEu_{0.02})Si_2O_2N_2$ phosphors could be efficiently excited by UV to blue light. To understand the effect of alkaline earth ion (Sr^{2+}/Ba^{2+}) substitution on Eu^{2+} luminescence in $(Sr_{0.98-x}Ba_xEu_{0.02})Si_2O_2N_2$, emission spectra were obtained under 405 nm UV excitation and Eu-doping concentration was fixed at 0.02. The corresponding CIE color coordinates calculated from their emission spectra (λ_{ex} = 405 nm) are shown in Figure 6a and Table 3, and the representative digital images of the studied samples under 365 nm UV light are shown in Figure 6b. In addition, the emission peaks and external quantum efficiencies (EQY) of the studied samples are also summarized in Table 3.

Generally, if Eu^{2+} randomly occupies cation positions in the host lattice, then the substitution of Sr^{2+} by larger Ba^{2+} ions causes a shift to shorter emission wavelengths because of the lower Eu^{2+} 5d-orbital splitting.[11,12b] Under 405 nm UV excitation, Eu-doped pure $Sr_{0.98}Si_2O_2N_2$ and $Ba_{0.98}Si_2O_2N_2$ show typical broadband emission resulting from the 5d−4f transition of Eu^{2+}, with maximum emission wavelengths of 536 nm (Figure 5b) and 494 nm (Figure 5c), respectively. These results are consistent with the calculated bond length result, which the average bond length of Ba−O (2.83 Å) in $Ba_{0.98}Si_2O_2N_2$ is longer than that of Sr−O (2.68 Å) in $Sr_{0.98}Si_2O_2N_2$. However, an obvious shift of an emission band from 536 to 571 nm is observed with the increase in Ba concentration from 0 to 0.63 (Figure 5b). The corresponding movement of color coordinates from green to yellow region (Figure 6, I) also verifies this red-shifted luminescence. With regard to a single phase (triclinic, $P1$) in phase 1 series, this unexpected red-shift may be due to the change in local environment of Eu^{2+}. Scheme 2 shows a possible red-shift luminescence mechanism, as explained by refs 11 and 12a. First, in a local structure, one Eu^{2+} occupies one Sr^{2+} site in phase 1

dx.doi.org/10.1021/cm500844v | Chem. Mater. 2014, 26, 2991−3001

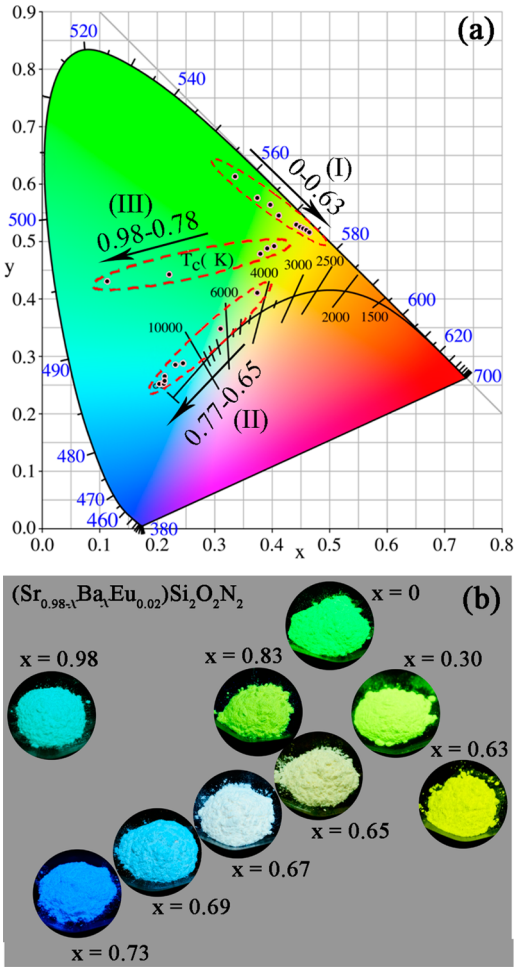

Figure 6. CIE color coordinate program of $(Sr_{0.98-x}Ba_xEu_{0.02})Si_2O_2N_2$ samples (λ_{ex} = 405 nm): (I) x = 0 to 0.63; (II) x = 0.65 to 0.77; and (III) x = 0.78 to 0.98.

series. The strain of the Ba−O bond increases when the neighboring Sr^{2+} ion is replaced by one larger Ba^{2+} ion (Scheme 2i). $EuSi_2O_2N_2$ is isotypic to $SrSi_2O_2N_2$, and the ion radius of Eu^{2+} (r = 1.20 Å, CN = 7) is similar to that of Sr^{2+} (^7r = 1.21 Å, CN = 7), indicating that a completely solid solution $(Eu/Sr)Si_2O_2N_2$ can be formed.[12b,19] Thus, Eu^{2+} dopants preferentially replace Sr^{2+} sites in $(Sr_{0.98-x}Ba_xEu_{0.02})Si_2O_2N_2$ (x = 0 to 0.63). To release lattice strain, the Eu−O bond length decreases (Scheme 2i). With the increase of Ba^{2+} content, other neighboring Sr^{2+} sites are successively replaced by Ba^{2+} ions (Schemes 2ii and 2iii), thereby gradually decreasing the Eu−O bond length. This phenomenon increases 5*d*-orbital crystal field splitting of Eu^{2+} ions, causing a continuous redshift in the emission spectra. To validate the hypothesis, the local fine structures of $(Sr_{0.98-x}Ba_xEu_{0.02})Si_2O_2N_2$ (x = 0 to 0.63) samples were characterized with the use of extended X-ray absorption spectra (Figure 7). Compared with the average bond lengths of Sr−Sr (3.71 Å), Sr−O (2.62 Å), and Sr−N (2.73 Å) bonds in the representative $Sr_{0.98}Eu_{0.02}Si_2O_2N_2$ (Rietveld refinement data in Table S6, Supporting Information), it can be determined that the Sr−O is the first coordination layer and the Sr−O/N is the second coordination layer. Moreover, the bond lengths of Sr−O and Sr−O/N bonds decrease with x increase in phase 1 series, as shown in Figure 7. This phenomenon indicates that the 5*d*-orbital crystal field

Table 3. CIE Color Coordinates, Emission Peaks, and External Quantum Efficiencies (EQY) of $(Sr_{0.98-x}Ba_xEu_{0.02})Si_2O_2N_2$ (x = 0 to 0.98) Samples (λ_{ex} = 405 nm)

	$(Sr_{0.98-x}Ba_xEu_{0.02})Si_2O_2N_2$	CIE x	CIE x	peak	EQY
I	x = 0	0.3364	0.6131	536	0.89
	x = 0.10	0.3749	0.5766	545	0.87
	x = 0.20	0.3967	0.5634	551	0.87
	x = 0.30	0.4124	0.5448	558	0.88
	x = 0.40	0.4428	0.5297	563	0.89
	x = 0.49	0.4497	0.5260	568	0.89
	x = 0.53	0.4550	0.5230	569	0.90
	x = 0.58	0.4594	0.5201	570	0.90
	x = 0.63	0.4655	0.5156	571	0.91
II	x = 0.65	0.3746	0.4180	473, 569	0.91
	x = 0.67	0.3106	0.3479	473, 569	0.84
	x = 0.69	0.2132	0.2574	473, 569	0.56
	x = 0.71	0.2124	0.2526	473	0.59
	x = 0.73	0.2042	0.2524	473	0.74
	x = 0.75	0.2138	0.2647	473	0.66
	x = 0.77	0.2318	0.2859	473	0.54
III	x = 0.78	0.4042	0.4925	494, 569	0.55
	x = 0.83	0.3923	0.4874	494, 567	0.55
	x = 0.88	0.3802	0.4788	494	0.57
	x = 0.93	0.2216	0.4424	494	0.57
	x = 0.98	0.1139	0.4305	494	0.60

Scheme 2. Schematic Explanation of Red-shift Luminescence Mechanism in Phase 1 Series (x = 0 to 0.63) and Blue Emission in Phase 2 Series (x = 0.68 to 0.77)

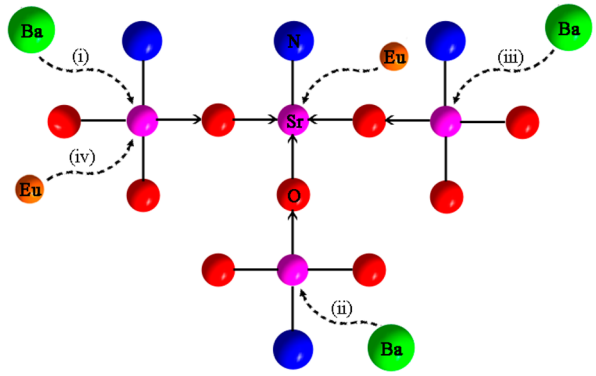

splitting of Eu^{2+} ions gradually increases with increasing x, thereby supporting the proposed red-shifted luminescence mechanism.

Figure 5c shows the emission spectra of $Sr_{0.98-x}Ba_xEu_{0.02}Si_2O_2N_2$ (x = 0.78 to 0.98) (λ_{ex} = 405 nm). The symmetrical emission band from 430 to 565 nm centered at 494 nm with a narrower full width at half-maximum (fwhm =48 nm) in $(Ba_{0.98}Eu_{0.02})Si_2O_2N_2$ is attributed to single Ba^{2+} site in the lattice. However, an additional emission peak appears when Ba^{2+} is substituted by Sr^{2+} in phase 3 series, which gradually strengthens with the increase of Sr^{2+} concentration. This finding indicates the presence of different luminescence centers of Eu^{2+} in lattice. The additional peak is located about 570 nm on the basis of the Gaussian fitting of the emission spectrum of the representative $(Ba_{0.93}Sr_{0.05}Eu_{0.02})Si_2O_2N_2$ sample. According to the Rietveld refinement results (Table 1), only a single orthorhombic phase (*Pbcn*) exists in phase 3

dx.doi.org/10.1021/cm500844v | *Chem. Mater.* 2014, 26, 2991−3001

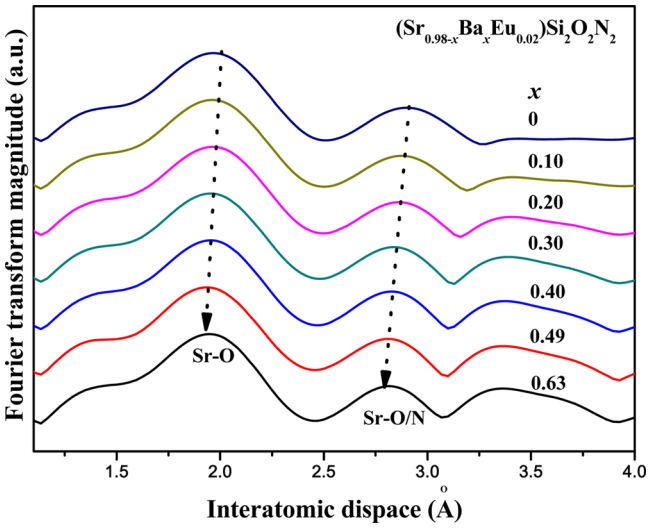

Figure 7. Extended X-ray absorption spectra of $(Sr_{0.98-x}Ba_xEu_{0.02})Si_2O_2N_2$ (x = 0 to 0.63) samples for the characterization of local fine structure.

series. Therefore, the additional luminescence center may result from the yellow emission of the local $(Sr/Eu)Si_2O_2N_2$ structure. This hypothesis is determined in view of the presence of the scattering angles of (2 1 0), (4 1 0), (6 1 0), and (8 1 0) at 10.36°, 14.92°, 20.40°, and 26.28°, respectively, in the XRD patterns of the phase 3 series. However, these peaks can not be found in the *Pbcn* space group. These indexes are confirmed by profile matching for the XRD pattern of the representative $(Ba_{0.93}Sr_{0.05}Eu_{0.02})Si_2O_2N_2$ assuming the *P1* symmetry (Figure S5a). Moreover, the peak widths of (2 1 0) and (4 1 0) are approximately twice that of the other peaks (Figure S5b). These observations yield additional evidence for the confirmation of the existence of $(Sr/Eu)Si_2O_2N_2$ nanoclusters. This result is similar to that in ref 12b, which ascribes the yellow luminescence to Eu^{2+}-doped triclinic $Sr_{0.5}Ba_{0.5}Si_2O_2N_2$ domains. Because the domains with different crystal structures present, the Eu atoms can locate in different surroundings. On the basis of the occupation of sites by Eu^{2+} in domains of different crystal structures (cyan emission at higher energy site and yellow emission at lower energy site), a color point tuning in single-phase host can be realized. With the increase in the Sr/Ba ratio in phase 3 series, more yellow-emitting Eu^{2+} sites appear, and the energy transfer might occur from higher-energy sites to lower-energy sites of Eu^{2+}. Therefore, the intensity of cyan emission gradually decreases, whereas the intensity of yellow emission gradually increases (Figure 5c). The corresponding CIE chromaticity coordinates of phase 3 series are tuned from the cyan region to the yellow region (Figure 6 and Table 3).

$(Sr_{0.98-x}Ba_xEu_{0.02})Si_2O_2N_2$ (x = 0.65 to 0.77) mainly shows blue emission band from 430 to 550 nm centered at 470 nm (Figure 5d). Other emission bands centered at 505 and ∼570 nm are also observed using Gaussian fitting of the representative $(Sr_{0.25}Ba_{0.73}Eu_{0.02})Si_2O_2N_2$. These emission bands are closely related to the change in coordination environment of the Eu^{2+} ions in phase 2 series. According to the NPD analysis, $(Sr_{0.25}Ba_{0.73}Eu_{0.02})Si_2O_2N_2$ presents three Ba^{2+} sites and one Sr^{2+} site. The average Ba−O bond lengths in the three Ba^{2+} sites are 2.85 Å (Ba1), 2.68 Å (Ba2), and 2.66 Å (Ba3), respectively, and the Sr−O bond length in the Sr^{2+} site is 2.72 Å. The corresponding values in $(Ba_{0.98}Eu_{0.02})Si_2O_2N_2$ and $(Sr_{0.98}Eu_{0.02})Si_2O_2N_2$ are 2.82 Å (Ba−O) and 2.65 Å (Sr−O). On the basis of r_{Ba1-O} (Phase 2) > r_{Ba-O} (Phase 3, cyan) > r_{Sr-O} (Phase 2) > r_{Sr-O} (Phase 1, green), we conclude that the blue emission at 473 nm and the blue-green emission at 505 nm might be caused by the dominant incorporation of Eu^{2+} into the Ba1 site (Scheme 2iv) and Sr^{2+} site, respectively. However, the emission band at ∼570 nm is similar to that in phase 3 series, which can be assigned to the yellow conversion of primary radiation by domains with the $(Sr/Eu)Si_2O_2N_2$ structure. The relative intensity of blue and yellow emissions can be adjusted in $(Sr_{0.98-x}Ba_xEu_{0.02})Si_2O_2N_2$ (x = 0.65−0.77) by changing the x values. Therefore, a color-tuning point from blue to yellow crossing the white light region is obtained (Figure 6 and Table 3). For example, white light with CIE color coordinates (0.3106, 0.3479) appears in single-compositional $(Sr_{0.31}Ba_{0.67}Eu_{0.02})Si_2O_2N_2$, which can be optimized further by adjusting the x values, thereby providing potential application as a single-compositional white-light-emitting phosphor in WLED.

In general, the tunable luminescence in the $(Sr_{0.98-x}Ba_xEu_{0.02})Si_2O_2N_2$ system is mainly due to the occupation of Eu^{2+} into domains with different crystal structures. In phases 1, 2, and 3 series, Eu^{2+} ions mainly occupy Sr^{2+}, Ba^{2+} (Phase 2), and Ba^{2+} (Phase 3) sites, respectively, leading to different local coordination environments around the Eu^{2+} ions, thereby producing different luminescence colors (Scheme 2). When the doping concentration of Ba is not more than that of Sr^{2+} ion in the matrix, the calculation results support the experimental conclusions about the chemical stress from Ba^{2+} ions on the local environment of Eu^{2+} ions based on the analyses of the crystal and electronic structures of $SrSi_2O_2N_2$, $Ba_{0.75}Sr_{0.25}Si_2O_2N_2$, and $BaSi_2O_2N_2$. The larger Stokes shift of the Ba^{2+} site rather than the Sr^{2+} site for luminescent Eu^{2+} ions is dominant, thereby producing a lower-energy d−f emission transition for Eu^{2+} when the Ba^{2+} ion content is larger than the Sr^{2+} ion content in the matrix. Thus, the two facts should be considered to illustrate the effect of microstructure on luminescence. This phenomenon provides understanding of the disorder on the site occupation behaviors of double-doped (Sr^{2+}-Ba^{2+}) ions, which will be explored in our subsequent study.

HRTEM and SAED Analyses. To verify the tunable luminescence in phase 2 (from blue to white) and phase 3 (from cyan to yellowish green), the $(Sr_{1-x}Ba_xEu_{0.02})Si_2O_2N_2$ samples were subjected to HRTEM and SAED experiments. In the $(Sr_{0.30}Ba_{0.68}Eu_{0.02})Si_2O_2N_2$ sample, the crystals were found to contain many nanocrystalline domains (Figure 8a). The d-spacings and interplanar angles vary in these domains. The structures of some domains match the triclinic unit cell of phase 1, namely, $(Sr_{0.35}Ba_{0.63}Eu_{0.02})Si_2O_2N_2$ with a = 7.228 Å, b = 7.429 Å, c = 7.352 Å, α = 88.65°, β = 84.42°, and γ = 75.92°. For example, the d-spacings of the top domain in Figure 8a are A = 2.91 Å, B = 5.14 Å, indexed to (−2−11) and (011), respectively, with an interplanar angle of 76.5°, which are similar to the calculated values (3.04 Å, 5.13 Å, and 78.5°, respectively). The marked bottom domain in Figure 8a shows d-spacings of C = 2.94 Å and D = 3.53 Å with an interplanar angle of 110°, which can be indexed to the triclinic unit cells of phase 2, namely, $(Sr_{0.23}Ba_{0.75}Eu_{0.02})Si_2O_2N_2$ with a = 4.804 Å, b = 5.462 Å, c = 14.302 Å, α = 89.70°, β = 90.04°, and γ = 89.59°. Consequently, the $(Sr_{0.30}Ba_{68}Eu_{0.02})Si_2O_2N_2$ sample can be regarded as the mixture of nanocrystalline domains of phases 1 and 2.

dx.doi.org/10.1021/cm500844v | *Chem. Mater.* 2014, 26, 2991−3001

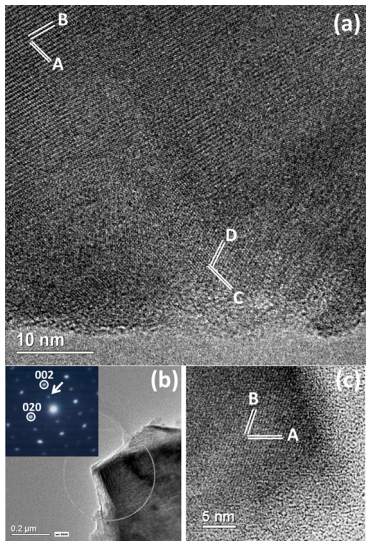

Figure 8. (a) Typical HRTEM image of $(Sr_{0.30}Ba_{0.68}Eu_{0.02})Si_2O_2N_2$ showing a domain structure. The *d*-spacings of two domains are marked. For the top domain, A = 2.91 Å, B = 5.14 Å, and the interplanar angle is 76.5°. For the bottom domain, C = 2.94 Å, D = 3.53 Å, and the interplanar angle is 110.0°. (b) TEM image of a particle from $(Sr_{0.15}Ba_{0.83}Eu_{0.02})Si_2O_2N_2$. The large circle shows the area where the SAED pattern was obtained (inset). The SAED pattern is indexed to the orthorhombic unit cell with a = 14.392 Å, b = 5.349 Å, and c = 4.835 Å. The interplanar angle between (002) and (020) is 90°. (c) HRTEM image of the orthorhombic structure with *d*-spacings A = 4.29 Å and B = 3.96 Å and interplanar angle of 107.5°.

By contrast, HRTEM images and SAED patterns of the $(Sr_{0.15}Ba_{0.83}Eu_{0.02})Si_2O_2N_2$ sample show an almost single phase 3. For example, the SAED pattern from a large area of a particle of this sample (Figure 8b) can be indexed to a pattern viewed on the [−100]. The interplanar angle between (002) and (020) is 90°. The diffraction spot of 001 is found, which should be systematically absent on the basis of the *Pbcn* space group, as determined from the XRD results. This phenomenon implies that the real structure may have lower symmetry. Figure 8c shows the HRTEM image of another particle from the same sample, in which the *d*-spacings are A = 4.29 Å and B = 3.96 Å with interplanar angle of 107.5°. These values are similar to the calculated *d*-spacings of (210): 4.29 Å and (−201): 4.02 Å, with an interplanar angle of 109.5° from the orthorhombic unit cell of $(Ba_{0.98}Eu_{0.02})Si_2O_2N_2$ with a = 14.392 Å, b = 5.349 Å, and c = 4.835 Å. However, several other particles from the sample can be identified as phase 2 with a composition of $(Sr_{0.35}Ba_{0.63})$-$Si_2O_2N_2$:2%Eu^{2+}. These results show that the crystal structure of this sample is attributed to the mixed phases of $(Sr_{0.35}Ba_{0.63}Eu_{0.02})Si_2O_2N_2$ and $(Ba_{0.98}Eu_{0.02})Si_2O_2N_2$ but may be closer to the latter phase. The HRTEM and ED results are consistent with the PL results. In general, the two kinds of luminescence tuning in phases 2 and 3 are attributed to nanophase segregation and mixing.

Thermal Quenching Properties. Thermal quenching behavior of phosphors is a critical factor in evaluating the importance of its application in WLED devices.[7c,14,21] Figure 9a shows the temperature-dependent emission spectra of the representative $(Sr_{0.98-x}Ba_xEu_{0.02})Si_2O_2N_2$ (x = 0, 0.63, 0.75, 0.98) samples in phase 1 to phase 3 series from 25 to 250 °C. For x = 0.73 sample, the emission peaks are basically persistent with temperature variation, indicating extra-high color stability. In x = 0, 0.63 samples, a slightly blue-shifted emission is found

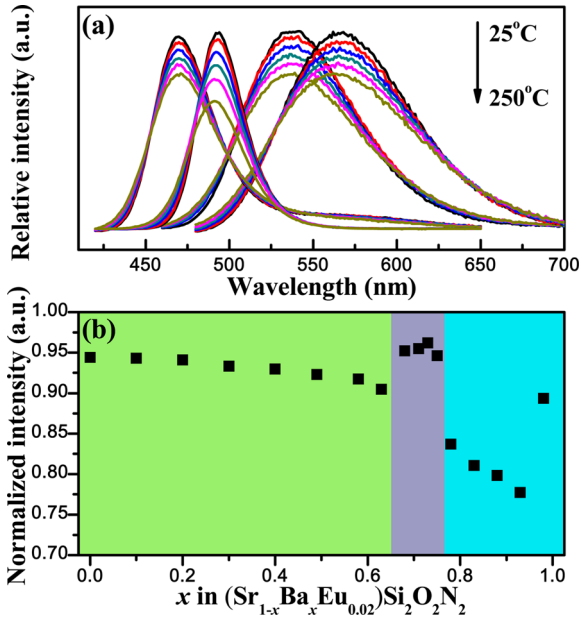

Figure 9. (a) Representative temperature-dependent emission spectra of $(Sr_{0.98-x}Ba_xEu_{0.02})Si_2O_2N_2$ (x = 0, 0.63, 0.75, 0.98) samples from 25 to 300 °C (solid line). (b) Comparison between the luminescence intensities of the $(Sr_{0.98-x}Ba_xEu_{0.02})Si_2O_2N_2$ samples at 200 °C, with respect to the original intensity at room temperature (25 °C).

with the temperature increase. This phenomenon is attributed to a relatively larger decay of Eu^{2+} emission in lower-energy sites than that in higher-energy sites. The comparison of luminescence decay of the entire $(Sr_{0.98-x}Ba_xEu_{0.02})Si_2O_2N_2$ systems at 200 °C is shown in Figure 9b. The emission intensity of phase 1 and phase 2 series at 200 °C remains >90% of the original intensity at 25 °C, particularly for phase 2 series (>95%), which is desirable for WLED applications. An increase in thermal quenching of luminescence is found in phase 1 series with the addition of Sr^{2+}. Given the same triclinic phase and *P1* space group, the difference in thermal quenching behavior in phase 1 and phase 2 series is related to the change in Stokes shift, which can be explained using the configuration coordinate diagram in Scheme 3.[22] In the simple harmonic oscillator model, the ground and excited states of Eu^{2+} can be described with parabolas, and overhead parabolas present three different excited states. As suggested, the electrons at excited states can be thermally excited with thermal energy $\Delta E_{1,\,2,\,3}$ to reach the

Scheme 3. Configuration Coordinate Diagram Showing the Thermal Quenching Caused by Stokes Shift in Phases 1 and 2 Series[a]

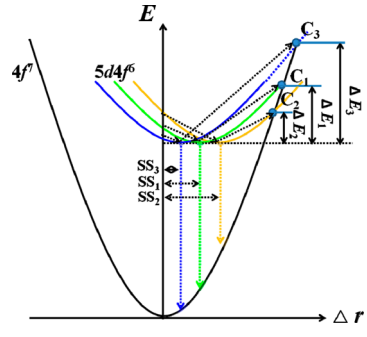

[a]SS, Stokes shift; C, crossing point; ΔE, thermal energy.

dx.doi.org/10.1021/cm500844v | Chem. Mater. 2014, 26, 2991−3001

crossing point $C_{1, 2, 3}$ of the three parabolas, respectively. These electrons then return to ground states, and the transition energy is released through heat dissipation rather than radiation emission, accompanied by the creation of a large number of phonons. Consequently, thermal quenching of luminescence occurs. Thermal energy decreases ($\Delta E_2 < \Delta E_1 < \Delta E_3$) with the increase in Stokes shift ($SS_2 > SS_1 > SS_3$), thereby are suggesting that the probability of nonradiative transition can be enhanced by thermal activation. Therefore, in phase 1 and phase 2 series, the thermal quenching behavior is as follows: blue-emitting materials > green-emitting materials > yellow-emitting materials. That is, smaller Stokes shift results in lower thermal luminescence quenching. In phase 3 series, for $x = 0.98$ sample, its emission spectra show a blue shift with elevating temperature from 25 to 250 °C (Figure 9a). The rigidity of lattice is weakened with the entrance of Eu^{2+} into Ba^{2+} sites because of a mismatch of ion radii. With the increase in temperature, the lattice expands and the connection force of Eu−O is gradually weakened, resulting in blue-shifted emission. Nevertheless, 89% of the original emission intensity is maintained, indicating that this material can be used as excellent cyan-emitter for WLED. A sudden increase in thermal quenching is observed when Sr^{2+} is introduced into the lattice ($x = 0.93$, ~78% of emission intensity at room temperature), which is slightly improved (relative to $x = 0.93$) with a further increase in Sr^{2+} content. This phenomenon may be appeared due to the slightly structural distortion in phase 3 series. A minimal amount of Ba^{2+} substitution by Sr^{2+} may result in a distortion of the neighboring Ba^{2+} (occupied by Eu^{2+}) sites because of the different coordinations of Sr^{2+} ions (trigonal prism) and Ba^{2+} ions (cuboid), which consequently undermine the Eu−O connection force, making Eu^{2+} ions easier to be disturbed and resulting in enhanced luminescent decay. The slight improvement in thermal quenching behavior in $Sr_{0.98-x}Ba_xEu_{0.02}Si_2O_2N_2$ ($x = 0.78$−0.93) with a continuous increase in Sr^{2+} content is due to the formation of yellow-emitting $(Sr/Ba)Eu_{0.02}Si_2O_2N_2$ domains, which have lower thermal quenching performance (Figure 9b). In addition, it is noticed that the as-prepared $(Sr_{1-x}Ba_x)Si_2O_2N_2$:Eu ($0 \le x \le 1$) phosphors have excellent reversible thermal behavior at the current Eu^{2+}-doping content. The luminescence intensities of all the as-prepared $(Sr_{1-x}Ba_x)Si_2O_2N_2$:Eu ($0 \le x \le 1$) phosphors can basically return to an original value within acceptable errors (<5%) after the temperature being return from 250 to 25 °C, which further exhibit their potential application in WLED devices.

■ CONCLUSION

In summary, oxonitridosilicate phosphors, $(Sr_{1-x}Ba_x)$-$Si_2O_2N_2$:Eu ($0 \le x \le 1$), were prepared using a simple two-step solid-state route. The XRD patterns and first-principle calculations indicate the variations in crystallinity upon substituting Ba^{2+} substitution by Sr^{2+}, revealing that the studied samples are divided into three sections [phase 1: ($x = 0$ to 0.63), phase 2 ($x = 0.68$ to 0.77), and phase 3 ($x = 0.78$ to 0.98)]. In phase 1, 2, and 3 series, Eu^{2+} ions occupy Sr^{2+}, Ba^{2+} (Phase 2), and Ba^{2+} (Phase 3) sites, respectively, which result in different local coordination environments around Eu^{2+} ions, thereby producing different luminescence. On the basis of the EXAFS analysis, the abnormal red shift is attributed to the Sr(Eu)-O/N bond length shrinkage in local structure. The blue emission is due to the main occupation of larger Ba1 sites by Eu^{2+} in phase 2 series. Interestingly, controllable luminescence from blue to white in phase 2 and from cyan to yellowish green in phase 3 were realized, which can be used to develop single-compositional white-emitting phosphor in blue and/or UV-based WLED. According to the HRTEM and SAED analyses, the two kinds of luminescence tuning should be attributed to nanophase segregation (the mixing of nanocrystalline domains). In addition, the studied samples show weak thermal quenching performance and the corresponding mechanisms were proposed. The tunable photoluminescent spectra and optimizing luminescent properties of oxonitridosilicates phosphors show their potential application in WLED devices. This study can serve as a guide in developing oxonitride materials with controllable optical properties based on the variation of local coordination environments through cation substitutions.

■ ASSOCIATED CONTENT

Ⓢ Supporting Information

Tables S1-S6 and Figures S1-S5. This material is available free of charge via the Internet at http://pubs.acs.org.

■ AUTHOR INFORMATION

Corresponding Author

*E-mail: rsliu@ntu.edu.tw.

Notes

The authors declare no competing financial interest.

■ ACKNOWLEDGMENTS

The authors would like to thank the Ministry of Science and Technology of Taiwan (Contract No. MOST 101-2113-M-002-014-MY3), the National Synchrotron Radiation Research Center, Taiwan, the National Natural Science Foundation of China (Grant No. NSFC 21301162), and the Fundamental Research Funds for the Central Universities (Grant No. CUG 130402) for financially supporting this research. Victor V. Atuchin gratefully acknowledges the Ministry of Education and Science of the Russian Federation for the financial support.

■ REFERENCES

(1) (a) Hoeppe, H. A. *Angew. Chem., Int. Ed.* **2009**, *48*, 3572. (b) Jüstel, T.; Nikol, H.; Ronda, C. *Angew. Chem., Int. Ed.* **1998**, *37*, 3084. (c) Nakamura, S.; Mukai, T.; Senoh, M. *Appl. Phys. Lett.* **1994**, *64*, 1687. (d) Schubert, E. F.; Kim, J. K. *Science* **2005**, *308*, 1274. (e) Lin, C. C.; Liu, R. S. *J. Phys. Chem. Lett.* **2011**, *2*, 1268.

(2) (a) Xie, R. J.; Hirosaki, N. *Sci. Technol. Adv. Mater.* **2007**, *8*, 588. (b) Zeuner, M.; Pagano, S.; Schnick, W. *Angew. Chem., Int. Ed.* **2011**, *50*, 7754. (c) Setlur, A. A. *Electrochem. Soc. Interface* **2009**, *18*, 32. (d) Shang, M. M.; Li, C. X.; Lin, J. *Chem. Soc. Rev.* **2014**, *43*, 1372.

(3) (a) Chen, Y.; Gong, M.; Wang, G.; Su, Q. *Appl. Phys. Lett.* **2007**, *91*, 071117. (b) Ten Kate, O. M.; Zhang, Z.; Dorenbos, P.; Hintzen, H. T.; Van der Kolk, E. *J. Solid State Chem.* **2013**, *197*, 209. (c) Jung, Y. W.; Lee, B.; Singh, S. P.; Sohn, K. S. *Opt. Exp.* **2010**, *18*, 17805.

(4) (a) Uheda, K.; Hirosaki, N.; Yamamoto, Y.; Naoto, A.; Nakajima, T.; Yamamoto, H. *Electrochem. Solid State Lett.* **2006**, *9*, H22. (b) Huang, C. H.; Chen, T. M. *Inorg. Chem.* **2011**, *50*, 5725.

(5) (a) Li, G. G.; Hou, Z. Y.; Peng, C.; Wang, W. X.; Cheng, Z. Y.; Li, C. X.; Lian, H. Z.; Lin, J. *J. Mater. Chem.* **2010**, *20*, 3446. (b) Li, G. G.; Li, C. X.; Zhang, C. M.; Cheng, Z. Y.; Quan, Z. W.; Peng, C.; Lin, J. *J. Mater. Chem.* **2009**, *19*, 8936. (c) Li, G. G.; Geng, D. L.; Shang, M. M.; Zhang, Y.; Peng, C.; Cheng, Z. Y.; Lin, J. *J. Phys. Chem. C* **2011**, *115*, 21882. (d) Huang, C. H.; Chiu, Y. C.; Yeh, Y. T.; Chan, T. S.; Chen, T. M. *ACS Appl. Mater. Interfaces* **2012**, *4*, 6661. (e) Xia, Z. G.; Zhang, Y. Y.; Molokeev, M. S.; Atuchin, V. V.; Luo, Y. 2013, DOI:10.1038/srep03310.

(6) (a) Park, W. B.; Singh, S. P.; Yoon, C.; Sohn, K. S. *J. Mater. Chem. C* **2013**, *1*, 1832. (b) Han, B. Y.; Sohn, K. S. *Electrochem. Solid State Lett.* **2010**, *13*, J62. (c) Seibald, M.; Rosenthal, T.; Oeckler, O.; Maak, C.; Tücks, A.; Schmidt, P. J.; Wiechert, D.; Schnick, W. *Chem. Mater.* **2013**, *25*, 1852. (d) Braun, C.; Seibald, M.; Börger, S. L.; Oeckler, O.; Boyko, T. D.; Moewes, A.; Miehe, G.; Tücks, A.; Schnick, W. *Chem.—Eur. J.* **2010**, *16*, 9646. (e) Oeckler, O.; Kechele, J. A.; Koss, H.; Schmidt, P. J.; Schnick, W. *Chem.—Eur. J.* **2009**, *15*, 5311. (f) Li, Y. Q.; van Steen, J. E. J.; van Krevel, J. W. H.; Botty, G.; Delsing, A. C. A.; Disalvo, F. J.; de With, G.; Hintzen, H. T. *J. Alloys Compd.* **2006**, *417*, 273. (g) Yun, B. G.; Horikawa, T.; Hanzawa, H.; Machida, K. I. *J. Electrochem. Soc.* **2010**, *157*, J364.

(7) (a) Zeuner, M.; Schmidt, P. J.; Schnick, W. *Chem. Mater.* **2009**, *21*, 2467. (b) Lee, B.; Lee, S.; Jeong, H. G.; Sohn, K. S. *ACS. Comb. Sci.* **2011**, *13*, 154. (c) Zhang, Z. J.; Ten Kate, O. M.; Delsing, A. C. A.; Stevens, M. J. H.; Zhao, J. T.; Notten, P. H. L.; Dorenbos, P.; Hintzen, H. T. *J. Mater. Chem.* **2012**, *22*, 23871. (d) Li, Y. Q.; Hirosaki, N.; Xie, R. J.; Takeda, T.; Mitomo, M. *Chem. Mater.* **2008**, *20*, 6704. (e) Uheda, K.; Hirosaki, N.; Yamamoto, Y.; Naito, A.; Nakajima, T.; Yamamoto, H. *Electrochem. Solid State Lett.* **2006**, *9*, H22. (f) Lee, S.; Sohn, K. S. *Opt. Lett.* **2010**, *35*, 1004.

(8) (a) Höppe, H. A.; Stadler, F.; Oeckler, O.; Schnick, W. *Angew. Chem., Int. Ed.* **2004**, *43*, 5540. (b) Oeckler, O.; Stadler, F.; Rosenthal, T.; Schnick, W. *Solid State Sci.* **2007**, *9*, 205. (c) Kechele, J. A.; Oeckler, O.; Stadler, F.; Schnick, W. *Solid State Sci.* **2009**, *11*, 537. (d) Seibald, M.; Rosenthal, T.; Oeckler, O.; Schmick, W. *Crit. Rev. Solid State* **2014**, *39*, 215.

(9) Li, Y. Q.; Delsing, A. C. A.; de With, G.; Hintzen, H. T. *Chem. Mater.* **2005**, *17*, 3242.

(10) (a) Li, Y. Q.; De With, G.; Hintzen, H. T. *J. Solid. State. Chem.* **2008**, *181*, 515. (b) Setlur, A. A.; Heward, W. J.; Hannah, M. E.; Happek, U. *Chem. Mater.* **2008**, *20*, 6277.

(11) Bachmann, V.; Ronda, C.; Oeckler, O.; Schnick, W.; Meijerink, A. *Chem. Mater.* **2009**, *21*, 316.

(12) (a) Seibald, M.; Oeckler, O.; Celinski, V. R.; Schmidt, P. J.; Tücks, A.; Schnick, W. *Solid State Sci.* **2011**, *13*, 1769. (b) Seibald, M.; Rosenthal, T.; Oeckler, O.; Fahrnbauer, F.; Tücks, A.; Schmidt, P. J.; Schnick, W. *Chem.—Eur. J.* **2012**, *18*, 13446.

(13) Bruker AXS *TOPAS V4*: General profile and structure analysis software for powder diffraction data. − User's Manual, Bruker AXS: Karlsruhe, Germany, 2008.

(14) Dovesi, R.; Saunders, V. R.; Roetti, C.; Orlando, R.; Zicovich-Wilson, C. M.; Pascale, F.; Civalleri, B.; Doll, K.; Harrison, N. M.; Bush, I. J.; D'Arco, P.; Llunell, M. *CRYSTAL09 User's Manual*; University of Torino: Torino, 2009.

(15) Demichelis, R.; Civalleri, B.; Ferrabone, M.; Dovesi, R. *Int. J. Quantum Chem.* **2010**, *110*, 406.

(16) (a) Pascale, F.; Zicovich-Wilson, C. M.; Orlando, R.; Roetti, C.; Ugliengo, P.; Dovesi, R. *J. Phys. Chem. B* **2005**, *109*, 6146. (b) Bredow, T.; Jug, K.; Evarestov, R. A. *Phys. Status Solidi B* **2006**, *243*, R10. (c) Gatti, C.; Saunders, V. R.; Roetti, C. *J. Chem. Phys.* **1994**, *101*, 10686.

(17) Piskunov, S.; Heifets, E.; Eglitis, R. I.; Borstel, G. *Comput. Mater. Sci.* **2004**, *29*, 165.

(18) (a) Stadler, F.; Oeckler, O.; Höppe, H. A.; Möller, M. H.; Pöttgen, R.; Mosel, B. D.; Schmidt, P.; Duppel, V.; Simon, A.; Schnick, W. *Chem.—Eur. J.* **2006**, *12*, 6984. (b) Yeh, C. W.; Chen, W. T.; Liu, R. S.; Hu, S. F.; Sheu, H. S.; Chen, J. M.; Hintzen, H. T. *J. Am. Chem. Soc.* **2012**, *134*, 14108.

(19) Shannon, R. D. *Acta Crystallogr.* **1976**, *A32*, 751.

(20) (a) Kohn, S.; Hoffbauer, W.; Jansen, M.; Franke, R.; Bender, S. *J. Non-Cryst. Solids* **1998**, *224*, 232. (b) Lauterbach, R.; Schnick, W. *Z. Anorg. Allg. Chem.* **1998**, *624*, 1154. (c) Schnick, W.; Huppertz, H.; Lauterbach, R. *J. Mater. Chem.* **1999**, *9*, 289. (d) KPllisch, K.; Schnick, W. *Angew. Chem.* **1999**, *111*, 368; *Angew. Chem., Int. Ed.* **1999**, *38*, 357. (e) Lauterbach, R.; Schnick, W. *Z. Anorg. Allg. Chem.* **2000**, *626*, 56. (f) Irran, E.; KPllisch, K.; Leoni, S.; Nesper, R.; Henry, P. F.; Weller, M. T.; Schnick, W. *Chem.—Eur. J.* **2000**, *6*, 2714. (g) Lauterbach, R.; Irran, E.; Henry, P. F.; Weller, M. T.; Schnick, W. *J. Mater. Chem.* **2000**, *10*, 1357. (h) Lauterbach, R.; Schnick, W. *Solid State Sci.* **2000**, *2*, 463. (i) Höppe, H. A.; Kotzyba, G.; Pöttgen, R.; Schnick, W. *J. Solid State Chem.* **2002**, *167*, 393.

(21) Xie, R. J.; Hirosaki, N.; Suehiro, T.; Xu, F. F.; Mitomo, M. *Chem. Mater.* **2006**, *18*, 5578.

(22) Liu, L. H.; Xie, R. J.; Hirosaki, N.; Takeda, T.; Li, J. G.; Sun, X. D. *J. Am. Ceram. Soc.* **2009**, *92*, 2668.